The Microphysics of Ice and Precipitation Development in Tropical Cumulus Clouds

R. Paul Lawson and Sarah Woods

SPEC Incorporated, Boulder, Colorado

Hugh Morrison

National Center for Atmospheric Research,* Boulder, Colorado

ABSTRACT

The rapid glaciation of tropical cumulus clouds has been an enigma and has been debated in the literature for over 60 years. Possible mechanisms responsible for the rapid freezing have been postulated, but until now direct evidence has been lacking. Recent high-speed photography of electrostatically suspended supercooled drops in the laboratory has shown that freezing events produce small secondary ice particles. Aircraft observations from the Ice in Clouds Experiment–Tropical (ICE-T), strongly suggest that the drop-freezing secondary ice production mechanism is operating in strong, tropical cumulus updraft cores. The result is the production of small ice particles colliding with large supercooled drops (hundreds of microns up to millimeters in diameter), producing a cascading process that results in rapid glaciation of water drops in the updraft. The process was analyzed from data collected using state-of-the-art cloud particle probes during 54 Learjet penetrations of strong cumulus updraft cores over open ocean in a temperature range from 5° to −20°C. Repeated Learjet penetrations of an updraft core containing 3–$5\,\mathrm{g\,m^{-3}}$ supercooled liquid showed an order-of-magnitude decrease in liquid mass concentration 3 min later at an elevation 1–1.5 km higher in the cloud. The aircraft observations were simulated using a one-dimensional cloud model with explicit bin microphysics. The model was initialized with drop and ice particle size distributions observed prior to rapid glaciation. Simulations show that the model can explain the observed rapid glaciation by the drop-freezing secondary ice production process and subsequent riming, which results when large supercooled drops collide with ice particles.

1. Introduction

The hydrologic cycle and atmospheric circulation in the tropics and extratropics has been a subject of interest for the past 60 years (Malkus 1954, 1957). Malkus and Ronne (1954) were the first to investigate the structure of cumulus clouds in the Caribbean using instrumented aircraft. Simpson et al. (1965) pioneered the development of numerical cumulus cloud models based on her work in the Caribbean. In 1974, 72 nations joined in the Global Atmospheric Research Program's (GARP) Atlantic Tropical Experiment (GATE) to investigate clouds and air motions in the tropics. The GATE project utilized an unprecedented 39 ships and 13 large research aircraft (Kuettner 1974; Rodenhuis 1974; Kuettner and Parker 1976). As technology has evolved, several additional major field campaigns have been launched in the tropics, coupled with observations from space and sophisticated cloud-resolving, mesoscale, and global models. Yet key issues central to understanding precipitation processes in tropical cumulus clouds still remain.

The initiation and rapid development of ice in tropical and extratropical maritime clouds[1] with tops warmer than −10°C has been a long-standing enigma in cloud physics research (Koenig 1963, 1965; Mossop et al. 1970;

---

[1] Here, we consider tropical and extratropical maritime cumulus clouds to be those with relatively warm bases (on the order of 18°–24°C) with an active coalescence process that produces supercooled millimeter-diameter drops in the updraft.

Hallett et al. 1978; Hobbs and Rangno 1990; Beard 1992). There has been much speculation in the literature surrounding the physical processes involved with both nucleation and development of ice in maritime updrafts. In situ measurements find that the concentrations of ice nuclei are much lower, often by orders of magnitude, than observed ice concentrations at temperatures warmer than −10°C (e.g., Koenig 1963, 1965; Mossop 1968; Mossop et al. 1970; Hobbs and Rangno 1985).

Perhaps an equally perplexing observation is how rapidly maritime updrafts in cumulus clouds glaciate once ice is formed. With rudimentary instrumentation, Koenig (1963) observed that high concentrations of ice and graupel were observed within 5–10 min after millimeter-diameter supercooled drops formed in clouds with tops warmer than −10°C. Koenig (1963, 1965) hypothesized that large supercooled drops underwent a freezing–breakup process that produced ice splinters, leading to an ice multiplication process. Hobbs and Rangno (1990) investigated small, polar maritime cumulus with more advanced instrumentation. They also observed that clouds with tops warmer than −12°C rapidly glaciated after supercooled drizzle drops formed. Relatively high ice concentrations in tropical cumulus clouds have also been postulated to occur through the Hallett and Mossop (1974) secondary ice production process (Hallett et al. 1978; Harris-Hobbs and Cooper 1987). On the other hand, Hobbs and Rangno (1990) argue that the Hallett–Mossop process takes too long to account for rapid glaciation in polar maritime clouds. In addition to the early observational studies (e.g., Koenig 1963; Hallett et al. 1978), some modeling studies have suggested that rapid freezing of supercooled raindrops occurs when they collide with small ice particles in tropical clouds (Cotton 1972a,b; Scott and Hobbs 1977).

The observations and numerical simulations presented in this paper strongly support the premise that initial freezing of large drops in strong tropical updrafts results in a secondary ice production process, followed by rapid glaciation due to the differences in fall velocities between large supercooled drops and much smaller ice particles.

2. Measurements

The in situ observations analyzed and presented in this paper were collected during the Ice in Clouds Experiment–Tropical (ICE-T) (Heymsfield and Willis 2014). ICE-T was staged from St. Croix, U.S. Virgin Islands in July 2011. The National Science Foundation (NSF) C-130 operated by the National Center for Atmospheric Research (NCAR) and the SPEC, Inc., Learjet penetrated growing cumulus clouds over the open ocean, at least 75 km from any islands, in the vicinity of St. Croix. The C-130 often made measurements below cloud base and up to its limiting altitude of approximately 23 000 ft MSL (~7000 m; about the −15°C level).

The Learjet was equipped with state-of-the-art sensors for investigating cloud microphysics. Instruments that are germane to this research include the following: a cloud particle imager (CPI; Lawson et al. 2001); a two-dimensional stereo (2D-S) probe (Lawson et al. 2006); an upgraded high-volume precipitation spectrometer (HVPS-3; Lawson et al. 1998); a fast forward-scattering spectrometer probe (FFSSP; Brenguier et al. 1998); a fast cloud droplet probe (FCDP; O'Connor et al. 2008); an Aventech, Inc., Aircraft Integrated Meteorological Measurement System (AIMMS-20) air motion system (Beswick et al. 2008); and a Rosemount total temperature probe and signal conditioner. The FCDP, FFSSP, 2D-S, and HVPS were all equipped with probe tips to reduce the effects of ice crystals shattering (Korolev et al. 2011; Lawson 2011); data collected by these probes were postprocessed using an interarrival time algorithm to remove shattered particles (Lawson 2011).

The 2D-S data were processed following the procedures described in appendix A in Lawson (2011). Following Lawson (2011), 2D-S images smaller than $365\,\mu m$ were processed with method "M4," which resizes out-of-focus "donuts" using the Korolev (2007) diffraction correction. Images larger than $365\,\mu m$ were processed using method "M1," which measures the image dimension along the direction of flight. Images with sizes between 365 and $445\,\mu m$ use weighted means of M1 and M4. The depth of field (DOF) for small 2D-S images ($<100\,\mu m$) was determined using the equation DOF = $\pm 8r^2/\lambda$ (Lawson et al. 2006), where r is particle dimension divided by 2 and λ is the laser wavelength ($0.78\,\mu m$). Sample volume is a direct function of DOF until the DOF reaches the dimension between the probe arms. The DOF of the 2D-S has recently been verified using a precision drop generator in SPEC's calibration laboratory. The HVPS images were processed using the M1 technique, and the DOF for the HVPS is equal to the distance between the probe arms for the smallest ($150\,\mu m$) particle. Liquid water content (LWC) in the all-liquid region is computed by adding the FFSSP LWC from 2 to $39\,\mu m$ to the LWC computed from $40\,\mu m$ to 3 mm assuming spherical drops based on diameter measured by the 2D-S and HVPS probes. The FFSSP and FCDP data were processed using techniques described in Brenguier et al. (1998). Ice water content (IWC) is computed using 2D-S images from 10 to $250\,\mu m$ via the Baker and Lawson (2006) area-to-mass relationship for ice crystals. The IWC from 2D-S and HVPS images larger than $250\,\mu m$ was computed assuming the particles are spherical graupel with an ice density of $0.5\,g\,m^{-3}$.

Temperatures reported here that represent cloud penetrations were measured outside of cloud prior to entry. Thus, the in-cloud temperature of an updraft core is likely to be higher than the referenced temperature outside of cloud. The Rosemount total temperature probe is known to read erroneously colder by 1°–2°C when the element is wet, which is likely in clouds with a liquid water content greater than about $1–2 \, g \, m^{-3}$ (Lawson and Cooper 1990; LeMone 1980). Even so, on a few occasions, the Rosemount probe measured a positive buoyancy of up to 3°C in an updraft core, suggesting that these tropical updraft cores can be very vigorous.

The C-130 was equipped with a suite of microphysics instruments that included cloud droplet probe (CDP; Lance et al. 2010), CPI, and 2D-S probes, along with inertial navigation system (INS)-based air motion, remote sensing (W-band Doppler radar and lidar), and aerosol instrumentation. This paper focuses on Learjet measurements, with only limited supporting (cloud base) measurements from the C-130 microphysical and air motion sensors.

The accuracy of AIMMS-20 vertical air velocity measurements has not been well quantified in the peer-reviewed literature. To conduct a dynamic evaluation, the Learjet and C-130 flew in a vertical stack during one mission in order to penetrate the same updraft cores on seven different occasions. The Learjet flew 500 m below the C-130, keeping visual contact until the C-130 entered cloud. The Learjet entered the same cloud 10–15 s later. A comparison of the vertical air velocity measurements and statistics from the two aircraft during three cloud penetrations of weak to moderate updrafts is shown in Fig. 1. The comparison in Fig. 1 suggests that the AIMMS-20 system on the Learjet measures slightly larger peak values than the C-130. The AIMMS-20 values averaged over the updraft cores are slightly larger, while the AIMMS-20 and INS measurements averaged over the entire cloud pass are in better agreement. The differences between the AIMMS-20 and INS measurements could be attributable to several instrumentation factors, or they could be from differences in the updraft characteristics separated by 500 m. Although not shown here, average vertical air velocity measurements from the C-130 downward-looking Doppler radar were in better agreement with the Learjet vertical velocity measurements than the INS measurements. It is not possible to assess the reasons for the differences based on these limited measurements.

The primary role of the Learjet in ICE-T was to penetrate fresh, growing cumulus updrafts in the temperature range from 0° to −10°C, and then climb rapidly and make repeated penetrations at higher levels in the same cloud. Thus, the Learjet crew targeted growing
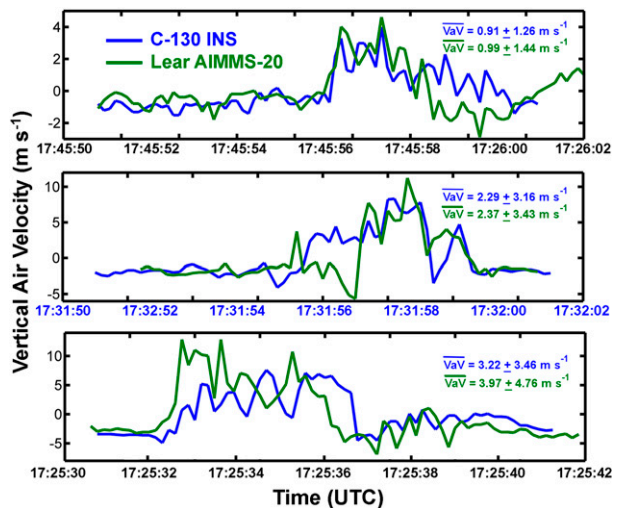

FIG. 1. Comparison of vertical air velocity (VAV) measured by the C-130 INS-based system and the Learjet AIMMS-20 during three cloud penetrations when the Learjet flew ~500 m below the C-130 and visually followed it by approximately 10–15 s into the same cloud turret (times of penetrations are offset by 11 s to achieve best overlap). Mean VAV and std dev for the cloud pass are shown in the upper-right portion of each panel.

turrets, often dashing up to clouds at maximum cruise speed in order to penetrate strong convection. The major scientific objective was to track the initiation and evolution of the ice phase in tropical, maritime cumulus clouds. Table 1 is a list of the times and general characterics from ICE-T updraft cores in growing clouds that were penetrated by the Learjet. The 54 updraft-core penetrations were selected from 137 Learjet cloud penetrations. The data in Table 1 also contain averages, maxima, and standard deviations for updraft cores that are segmented according to temperature ranges in the cloud. To qualify as an updraft core, the cloud pass had to have a region that was a minimum of 3 s ($\sim 0.5 \, km$) in duration with an average vertical velocity of $3 \, m \, s^{-1}$. The large majority of these updraft cores were larger and stronger than the minimum required for selection. The average updraft-core velocity in the −3° to −15°C region was about $10 \, m \, s^{-1}$, and the maximum 1-s peak updraft velocity was $25.4 \, m \, s^{-1}$. Table 2 shows mean values of the updraft-core measurements listed in Table 1 for cloud-base, all-liquid, first ice, and rapid glaciation regions. Mean values are weighted by duration time.

The data collected in updraft cores presented in Table 1 have larger average vertical velocities than previously observed in tropical cumulus clouds (e.g., Lucas et al. 1994). However, the previous average measurements were not presented as the strongest updraft cores in the dataset and were also collected by large turboprop aircraft, which do not have the dash speed and maneuverability

TABLE 1. List of measurements from updraft cores (as defined in the text). C130 in the date column indicates data collected by the NSF/NCAR C-130; all other data are collected by the SPEC Learjet. VaV is vertical air velocity and Z is equivalent radar reflectivity calculated from the particle size distribution (Lawson and Zuidema 2009). Mean values are at the end of each section are weighted by duration time.

Date	Time (UTC)	Temp (°C)	VaV mean (m s^{-1})	VaV max (m s^{-1})	VaV std dev (m s^{-1})	VaV duration (s)	Drop concentration (cm^{-3})	LWC (g m^{-3})	Liquid Z (dBZ)	Ice concentration (L^{-1})	IWC (g m^{-3})	Ice Z (dBZ)
						Cloud-base region						
12 Jul 2011 (C130)	1637:41–1637:47	22	1.3	1.9	0.5	7	161	0.3				
12 Jul 2011 (C130)	1637:50–1637:55	22	1.1	2.1	0.8	6	125	0.2				
12 Jul 2011 (C130)	1639:00–1639:04	22	0.7	1.1	0.3	5	109	0.2				
12 Jul 2011 (C130)	1639:31–1639:32	22	0.9	1.3	0.6	2	148	0.3				
12 Jul 2011 (C130)	1643:28–1643:33	22	0.8	1.2	0.4	6	172	0.3				
12 Jul 2011 (C130)	1643:37–1643:52	22	0.7	1.3	0.4	16	117	0.1				
12 Jul 2011 (C130)	1646:53–1647:03	22	0.6	1.0	0.2	11	161	0.1				
23 Jul 2011	1404:35–1404:41	23	1.2	2.2	0.7	7	116	0.3				
23 Jul 2011	1406:25–1406:29	23	0.4	0.5	0.2	5	71	0.1				
23 Jul 2011	1410:13–1410:15	23	0.9	1.1	0.2	3	109	0.4				
23 Jul 2011	1411:07–1411:12	23	0.9	2.0	0.9	6	74	0.2				
23 Jul 2011	1413:20–1413:25	23	0.8	1.8	0.7	6	61	0.2				
24 Jul 2011	2138:57–2139:03	22	2.5	3.4	0.9	7	62	0.1				
24 Jul 2011	2140:33–2140:35	22	1.5	2.2	0.6	3	50	0.1				
24 Jul 2011	2141:05–2141:10	22	1.6	1.8	0.2	6	33	0.1				
24 Jul 2011	2141:50–2141:54	22	1.8	2.4	0.5	5	31	0.1				
27 Jul 2011 (C130)	1721:59–1722:03	24	0.2	0.6	0.3	5	54	0.1				
27 Jul 2011 (C130)	1723:38–1723:46	22	0.7	1.9	0.6	9	49	0.2				
27 Jul 2011 (C130)	1726:04–1726:16	23	0.7	1.3	0.5	13	102	0.2				
27 Jul 2011 (C130)	1732:29–1732:35	21	2.2	4.4	1.5	7	160	0.6				
27 Jul 2011 (C130)	1742:46–1742:49	20	0.5	1.4	0.6	4	10	0.0				
28 Jul 2011 (C130)	1650:07–1650:10	23	0.9	1.5	0.5	4	127	0.3				
28 Jul 2011 (C130)	1650:15–1650:19	23	1.0	1.7	0.7	5	128	0.3				
28 Jul 2011 (C130)	1650:25–1650:29	23	1.1	2.2	0.6	5	78	0.1				
28 Jul 2011 (C130)	1659:38–1659:43	23	0.6	0.9	0.2	6	15	0.0				
28 Jul 2011 (C130)	1659:58–1700:01	22	0.4	1.0	0.4	4	12	0.0				
28 Jul 2011 (C130)	1700:42–1700:44	22	0.6	0.8	0.1	3	39	0.1				
28 Jul 2011 (C130)	1701:02–1701:06	22	0.7	1.3	0.5	5	30	0.1				
28 Jul 2011 (C130)	1703:24–1703:27	22	0.3	0.8	0.5	4	35	0.1				
28 Jul 2011 (C130)	1702:52–1702:54	22	0.5	0.9	0.5	3	35	0.1				
28 Jul 2011 (C130)	1704:21–1704:23	22	0.7	1.2	0.5	3	25	0.0				
Cloud-base region means		22	1.0	1.7	0.5	7	89	0.2				
						All-liquid region						
12 Jul 2011	1848:03–1848:12	−8	8.8	13.7	2.5	10	35	2.1	34			
12 Jul 2011	1916:43–1916:48	5	4.6	5.8	0.7	6	43	3.0	34			
15 Jul 2011	1605:03–1605:11	5	6.6	9.6	1.5	9	192	2.0	24			

TABLE 1. (*Continued*)

Date	Time (UTC)	Temp (°C)	VaV mean (m s⁻¹)	VaV max (m s⁻¹)	VaV std dev (m s⁻¹)	VaV duration (s)	Drop concentration (cm⁻³)	LWC (g m⁻³)	Liquid Z (dBZ)	Ice concentration (L⁻¹)	IWC (g m⁻³)	Ice Z (dBZ)
15 Jul 2011	1641:58–1642:03	−1	7.4	12.0	2.5	6	70	2.3	37			
15 Jul 2011	1702:48–1703:04	3	10.4	14.6	3.4	17	83	1.9	34			
19 Jul 2011	1936:04–1936:08	−8	9.3	13.8	3.6	5	37	1.5	29			
28 Jul 2011	1600:44–1601:13	−7	10.5	18.3	3.8	30	36	6.0	44			
28 Jul 2011	1605:38–1605:47	−7	14.8	23.0	5.3	10	20	4.4	43			
30 Jul 2011	1732:58–1733:02	−7	5.5	6.4	0.5	5	20	2.7	35			
All-liquid region means		−3	9.5	14.9	3.1	16	58	3.5	37			
						First ice region						
11 Jul 2011	1909:17–1909:20	−9	7.2	9.7	2.2	4	23	1.5	28	105	0.02	−16
12 Jul 2011	1818:50–1818:57	−8	9.2	12.4	2.5	8	42	2.0	31	9	0.00	−32
12 Jul 2011	1823:16–1823:24	−10	11.9	14.8	2.2	9	66	1.2	23	3	0.00	−24
12 Jul 2011	1826:34–1826:37	−11	6.1	6.7	0.6	4	60	0.9	22	6	0.00	−40
12 Jul 2011	1850:43–1850:53	−8	6.4	10.9	2.2	11	58	1.2	27	1	0.00	−51
19 Jul 2011	1936:10–1936:17	−8	9.9	13.9	2.9	8	34	1.9	33	26	0.00	−42
23 Jul 2011	1533:07–1533:20	−10	12.0	18.0	3.9	14	26	2.5	33	80	0.00	−38
27 Jul 2011	1910:10–1910:21	−9	11.5	20.8	4.4	12	26	3.4	40	108	0.02	−15
28 Jul 2011	1612:16–1612:25	−11	11.5	25.4	7.0	10	53	1.5	33	39	0.00	−26
30 Jul 2011	1720:14–1720:21	−8	13.2	18.8	3.4	8	10	4.5	39	101	0.03	−14
30 Jul 2011	1725:58–1726:21	−9	10.1	16.8	3.5	24	27	3.3	37	52	0.00	−30
First ice region means		−9	10.3	16.4	3.5	13	37	2.4	33	50	0.01	−31
						Rapid glaciation region						
6 Jul 2011	1833:38–1833:43	−13	6.3	7.5	1.6	5	55	0.3	−14	129	0.74	5
6 Jul 2011	1837:09–1837:19	−13	5.8	8.1	1.1	10	20	0.0	−22	230	1.21	8
11 Jul 2011	1836:39–1836:51	−17	6.0	10.2	2.0	12	33	0.2	−11	430	1.85	9
11 Jul 2011	1847:24–1847:32	−16	5.7	8.5	1.2	9	18	0.1	−11	284	2.16	15
11 Jul 2011	1856:47–1856:49	−18	8.8	9.6	0.9	3	40	0.3	−13	447	2.88	17
11 Jul 2011	1905:19–1905:25	−13	4.6	5.6	0.5	6	24	0.1	−19	239	1.53	15
12 Jul 2011	1831:41–1831:46	−17	7.6	11.0	2.6	5	51	0.3	−13	332	1.48	16
15 Jul 2011	1614:37–1614:55	−15	9.8	14.6	2.7	19	17	0.3	−11	1020	1.64	12
15 Jul 2011	1617:25–1617:38	−19	8.7	14.7	4.4	13	6	0.2	−8	1301	4.77	21
15 Jul 2011	1620:26–1620:29	−20	6.8	7.7	0.7	3	3	0.0	−27	987	7.30	24
15 Jul 2011	1620:32–1620:40	−20	13.9	21.0	5.4	8	22	0.2	−14	1630	5.17	23
15 Jul 2011	1620:41–1620:44	−20	7.8	13.3	3.9	3	10	0.1	−28	1051	5.32	20
19 Jul 2011	1925:30–1925:35	−18	4.9	6.2	0.7	5	7	0.0	−33	386	3.46	11
19 Jul 2011	1939:43–1939:46	−12	6.6	7.7	0.9	3	34	0.3	−9	391	0.78	5
23 Jul 2011	1449:42–1449:48	−12	6.6	8.8	1.5	6	23	0.3	−15	341	1.52	10
23 Jul 2011	1449:49–1449:57	−12	7.6	9.4	1.6	8	39	0.4	−15	317	1.48	10
23 Jul 2011	1456:06–1456:17	−15	6.4	10.4	1.7	11	27	0.2	−16	545	2.01	9

TABLE 1. (*Continued*)

Date	Time (UTC)	Temp (°C)	VaV mean (m s⁻¹)	VaV max (m s⁻¹)	VaV std dev (m s⁻¹)	VaV duration (s)	Drop concentration (cm⁻³)	LWC (g m⁻³)	Liquid Z (dBZ)	Ice concentration (L⁻¹)	IWC (g m⁻³)	Ice Z (dBZ)
23 Jul 2011	1458:54–1459:00	−14	7.5	9.7	2.0	6	22	0.3	−13	395	1.58	10
23 Jul 2011	1459:09–1459:19	−14	9.5	12.8	2.6	10	25	0.8	0	385	1.36	9
23 Jul 2011	1500:06–1500:16	−15	9.9	14.7	2.6	11	24	1.2	7	97	0.67	5
23 Jul 2011	1503:08–1503:13	−14	6.2	7.4	1.3	5	26	0.4	−10	770	2.23	10
27 Jul 2011	1522:49–1522:57	−14	4.7	5.8	0.7	8	4	0.0	−23	518	5.03	20
27 Jul 2011	1522:58–1523:02	−14	4.2	5.2	0.6	4	5	0.0	−28	318	3.90	16
27 Jul 2011	1525:52–1525:56	−17	9.4	14.1	2.7	5	68	1.0	6	434	0.71	4
27 Jul 2011	1529:23–1529:39	−15	7.7	16.8	3.5	17	15	0.1	−16	664	4.49	19
27 Jul 2011	1529:41–1529:45	−15	5.1	7.8	1.5	5	4	0.1	−14	1260	7.66	24
27 Jul 2011	1532:24–1532:31	−17	5.5	8.7	1.8	7	1	0.0	−16	345	4.30	19
27 Jul 2011	1608:06–1608:09	−19	9.5	15.3	4.3	3	26	0.3	−16	980	7.93	23
27 Jul 2011	1856:05–1556:12	−12	5.8	10.1	2.5	7	43	0.5	−6	151	0.41	6
27 Jul 2011	1901:48–1901:52	−15	3.9	5.2	0.7	4	3	0.0	−23	402	4.55	17
27 Jul 2011	1901:53–1901:56	−15	4.5	6.2	1.2	3	2	0.0	−31	451	7.72	20
27 Jul 2011	1912:34–1912:41	−14	4.7	6.0	1.0	7	37	0.1	−14	813	1.60	13
27 Jul 2011	1915:34–1915:37	−17	7.5	8.7	0.9	3	8	0.1	−15	732	3.71	21
28 Jul 2011	1620:15–1620:23	−13	9.2	16.8	3.3	8	8	0.0	−14	71	1.78	17
Rapid glaciation region means		−15	7.4	11.2	2.2	9	22	0.3	−13	572	2.78	14

TABLE 2. Mean values of the updraft-core measurements listed in Table 1 for each temperature region. Mean values are weighted by duration time. The equivalent radar reflectivity Z is calculated from the particle size distribution (Lawson and Zuidema 2009).

					VAV	VAV	Drop			Ice		
	Temp	VAV mean	VAV max	std dev	duration	concentration	LWC	Liquid Z	concentration	IWC	Ice Z
Region	(°C)	(m s^{-1})	(m s^{-1})	(m s^{-1})	(s)	(cm^{-3})	(g m^{-3})	(dBZ)	(L^{-1})	(g m^{-3})	(dBZ)
Cloud base	22	1.0	1.7	0.5	7	89	0.2				
All liquid	−3	9.5	14.9	3.1	16	58	3.5	37	0	0.00	0
First ice	−9	10.3	16.4	3.5	13	37	2.4	33	50	0.01	−31
Rapid glaciation	−15	7.4	11.2	2.2	9	22	0.3	−13	572	2.78	14

Header row spanning "ICE-T updraft-core mean values" across table.

of the Learjet. In contrast, Anderson et al. (2005) examine the 10% strongest updraft cores penetrated by a Citation research aircraft near Kwajalein and report values commensurate with data shown in Table 1. Heymsfield et al. (2010) show vertical profiles of maximum updraft velocity from airborne Doppler radar measurements. The updraft-core averages in Table 1 compare well with the average peak updraft velocities over ocean seen in Fig. 12 in Heymsfield et al. (2010).

The crew on the Learjet, which included experienced cloud physicists, identified clouds that were in their developmental stage, had cloud tops that were estimated to be warmer than about −12°C, and did not appear to be contaminated from clouds aloft or from neighboring clouds. However, the clouds in the ICE-T project tended to form in clusters that were attached near their bases; thus, the clouds were not entirely isolated. The cloud clusters often eventually developed into mature cumulonimbus with anvils. When this occurred, the aircraft would typically work more isolated cells near the storm or relocate to another cloud cluster.

Figure 2 shows an example of data collected from repeated Learjet penetrations of the same ICE-T cloud on 19 July 2011. The data in Fig. 2 were collected in the updraft core in each turret, which had a peak vertical velocity of 14 m s^{-1} at −8°C, 8 m s^{-1} at −12°C, and 4 m s^{-1} at −15°C. The middle panel in Fig. 2 shows very good overlap in particle size distributions (PSDs) from the FFSSP, 2D-S, and HVPS, which provides confidence in the measurements. CPI images were used to distinguish ice particles from water drops in the size region from 30 to 500 μm, and percentages of ice and water were then applied to the 2D-S PSD in that region. Images of particles smaller than 30 μm are assumed to be water drops. 2D-S images larger than 500 μm were inspected visually to estimate whether they were spherical or not spherical and categorized as ice or water; percentages were applied to the 2D-S and HVPS PSDs. In this way, composite PSDs were obtained for both ice particles and water drops and are displayed in the right panel of Fig. 2, along with total particle concentration and liquid and ice water contents derived from the respective PSDs.

The measurements in Fig. 2 show that the first ice that was observed near the −8°C level consisted of small (<100 μm) irregular-shaped ice particles in relatively low concentration (26 L^{-1}) compared with the concentration of water drops (34 cm^{-3}). The concentration of ice particles was derived from 3517 CPI images in the 8-s core of the updraft, which represents a small sample statistic of ice particles. For example, if three more ice particles were observed, the ice concentration would double, and if three fewer ice particles were observed, the concentration of ice would be zero. Thus, the actual number concentration of ice observed in the "first ice region" is not statistically significant, but it is very small compared with cloud penetrations at colder regions in the cloud shown in Fig. 2, where there is obviously a high concentration of ice, and the ice particle counting statistics are robust.

To improve sampling statistics, cloud penetrations were grouped according to temperature regions within the clouds. Because of the inherent low vertical velocities at cloud base, the definition of updraft cores is relaxed, and the cloud-base data in Table 1 are representative of the region where the average vertical air velocity was >0 m s^{-1}. Figure 3 shows drop size distributions (DSDs) from C-130 and Learjet penetrations that were conducted in updrafts within 200 m above the visual bases of ICE-T clouds. There are more C-130 measurements because it spent more time than the Learjet investigating the region below and just above the cloud base. The DSD measurements in Fig. 3 are a combination of CDP and 2D-S measurements on the C-130 and FFSSP and 2D-S measurements on the Learjet. The diameters of drops in updrafts within 200 m of cloud base extend out to 90 μm. The very broad cloud-base DSDs are an indication of the maritime composition of the cloud condensation nucleus (CCN) aerosols. It is noteworthy that cloud-base DSDs measured by the Learjet and C-130 are in good agreement.

Figure 4 shows Learjet 2D-S images and DSDs from penetrations of ICE-T updrafts in the all-liquid
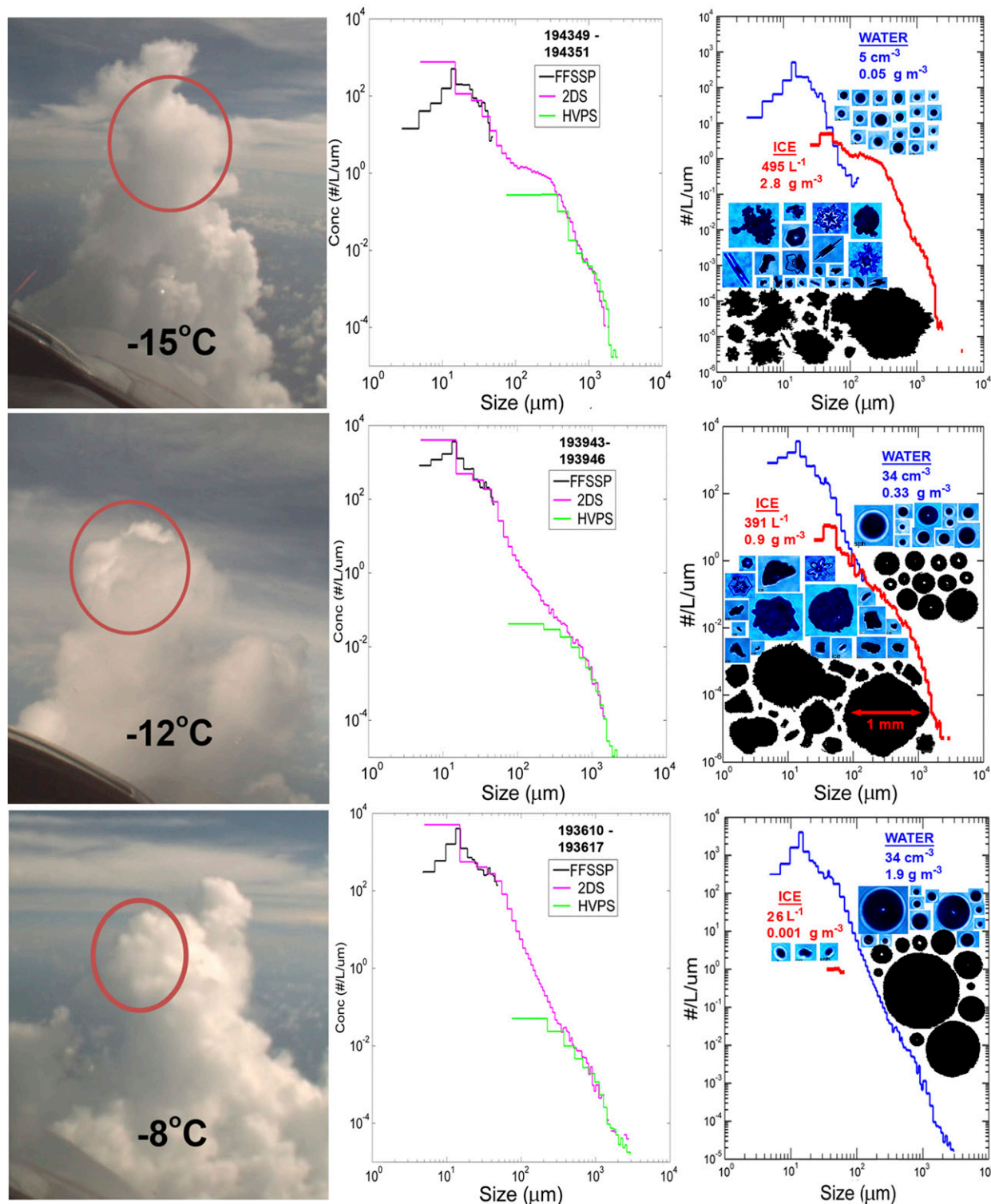
FIG. 2. Examples of (left) forward-facing video photos of locations (center of red circles) of repeated Learjet penetrations of the same cloud at three temperature levels; (middle) particle size distributions from three cloud particle probes on the aircraft; and (right) composite size distributions of water drops (blue) and ice particles (red). Examples of CPI and 2D-S images are shown along with values of particle number concentration (L^{-1}) and mass concentration ($g\,m^{-3}$) averaged over the updraft core.
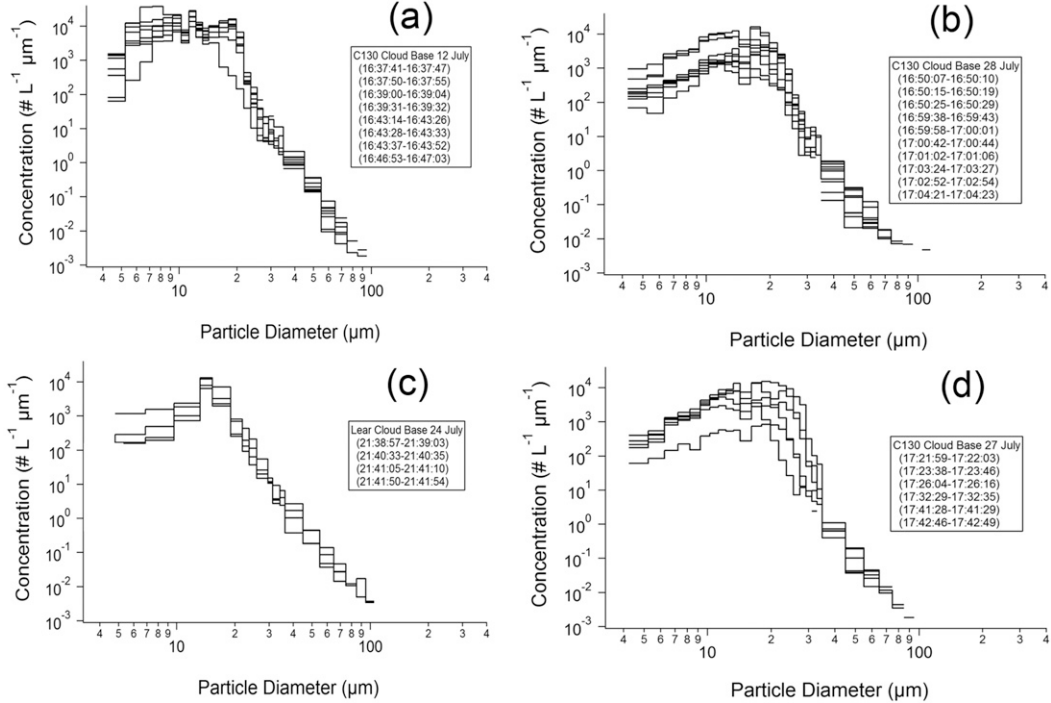
FIG. 3. Average drop size distributions measured by (a),(b),(d) C-130 and (c) Learjet penetrations in updrafts (average vertical velocity $> 0\,\mathrm{m\,s^{-1}}$) within 200 m above cloud base.

temperature region from 5° to −8°C. The all-liquid region is qualified by visual inspection to determine that there are no ice particles imaged on either the CPI or 2D-S probes. Nonspherical CPI images that are larger than about 30 μm (13-pixel diameter) are considered to be ice. Ice particles will grow at a minimum rate of about 1 μm s^{-1} at these temperatures in a water-saturated environment (Pruppacher and Klett 1997). Korolev et al. (2004) show that frozen drops in an environment near water saturation will diverge from a perfectly spherical shape within about a minute and be detected as ice.[2] The 2D-S images are used to detect much larger ice particles, such as graupel, which can be seen as nonspherical with its 10-μm-pixel resolution.

The average DSD in the all-liquid region shows that 1-mm-diameter drops were observed in the updrafts in concentrations $>1\,\mathrm{L^{-1}}$, which reflects the broad DSD at cloud base and a very active coalescence process. The average total drop concentration in the all-liquid region is 58 cm^{-3}, which is also reflective of a maritime DSD.

The average LWC computed from integrating the updraft-core average DSD was 3.5 g m^{-3} and the maximum LWC was 6 g m^{-3} (Table 1). For a cloud-base temperature of 22°C, the adiabatic LWC from 5° to −8°C increases from 7.0 to 7.8 g m^{-3}. These are relatively high values for developing cumulus clouds and suggest that entrainment was not a major factor in the lower regions of clouds. It is important to recall that many of the clouds were linked in the lower regions, so entrainment at these levels would not cause drops to evaporate.

Figure 5 shows PSDs from the temperature region between −8° and −12°C, where the first ice was observed. The first ice region still contains high LWC and about 1 L^{-1} of millimeter-diameter drops but only a few small ice particles, as shown in the example CPI images identified in Fig. 5 by red ellipses. Figure 6 shows CPI images of all of the ice observed in the first ice region. It is curious that even though these images are found in the midst of strong updrafts, not near cloud edges where downdrafts are typically observed, none of the ice appears to be faceted, as would be expected if grown via vapor deposition.

Leisner et al. (2014) show high-speed light microscopy of two mechanisms of secondary ice formation during the freezing of electrostatically suspended drops. One mechanism is from splintering of the freezing drop with large drop pieces and microscopic pieces produced during the freezing process. The second mechanism is

---

[2] Here, we note that Korolev et al. (2004), based on laboratory experiments, report that frozen drops maintain a quasi-spherical shape for tens of seconds after freezing near water saturation. However, the laboratory photographs suggest that protrusions would be detectable in CPI images within about 30 s after freezing in a water-saturated environment.
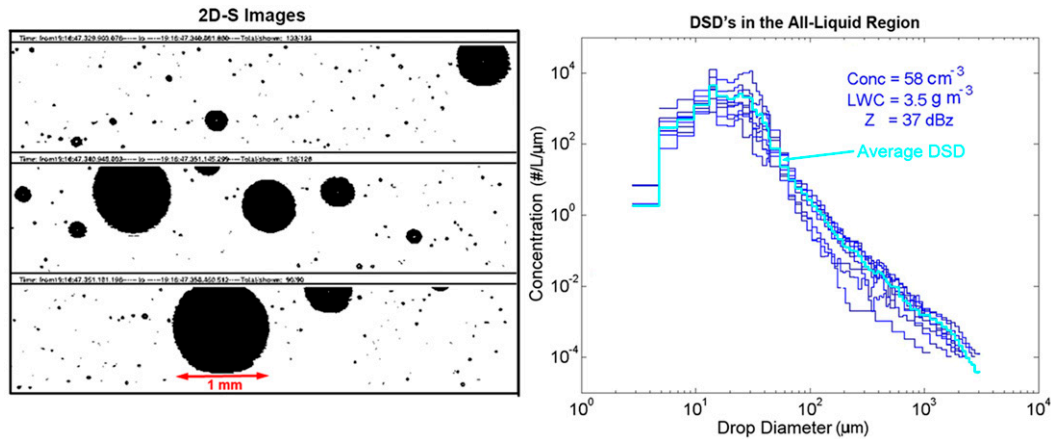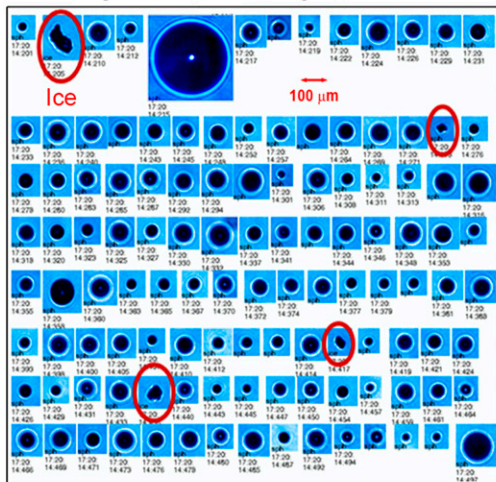
FIG. 4. (left) Examples of 2D-S images in an updraft core at 5°C at 1916:47 UTC 12 Jul 2011, and (right) DSDs from all penetrations in the all-liquid region shown in Table 1. The average values of drop concentration (Conc), LWC, and equivalent radar reflectivity (Z) are shown along with the time-weighted average of all DSDs (cyan).

the formation of spicules and subsequent ejection of gas bubble membranes that break into ice fragments. As shown in Fig. 7, freezing drops can either break up into fragments or form spicules that eject membrane bubbles that break and form several ice fragments. The spicules form because the outer shell of the drop freezes first, while the slushy interior freezes more slowly, resulting in internal pressure as the ice expands and forces a spicule to form through the exterior shell. Leisner et al. (2014) found that particles immersed in the drops (not necessarily active ice nuclei) enhanced the spicule formation

process and that more than 10% of the freezing drops produce secondary ice.

We are not postulating that the drop breakup and/or spicule ice-formation mechanisms are also responsible for the formation of first ice. These processes or some primary nucleation process (e.g., biogenic ice forming nuclei) could produce the first ice. It is not possible to conclusively determine the origin of first ice in these clouds. The data presented here only show that the first detectable ice particles are irregular in shape and that some appear to be fragments of broken drops.
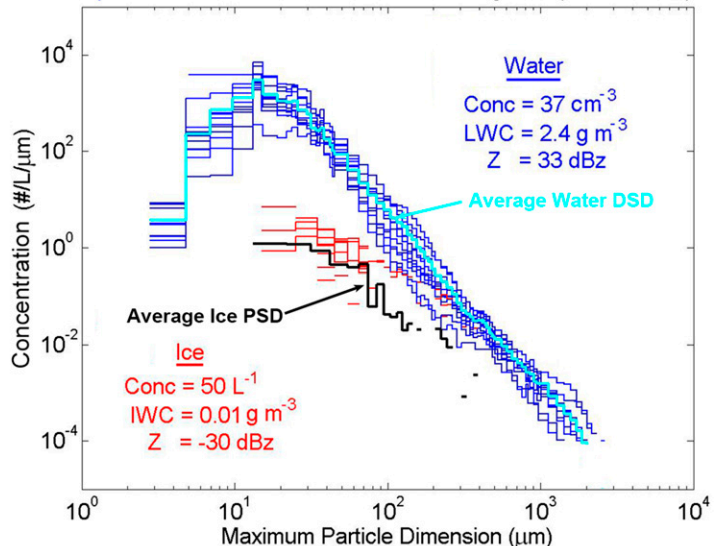
FIG. 5. (left) Examples of CPI images in an updraft core at −8°C at 1720:14 UTC 30 Jul 2011. Red ellipses indicate irregular shapes that are designated as ice. (right) Size distributions from all penetrations in the first ice region shown in Table 1. Average values of drop concentration (blue Conc), ice concentration (red Conc), LWC, IWC, and equivalent water (blue) and ice (red) radar reflectivity (Z) are shown along with the time-weighted average of all DSDs (light blue), and the time-weighted average of all ice PSDs (black).
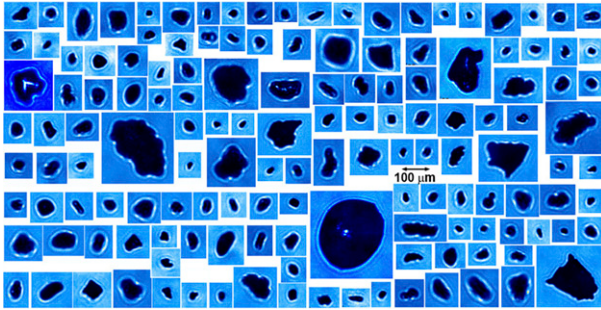
FIG. 6. CPI images of all particles that were classified as ice in the first ice region shown in Table 1.

Several investigators have observed spicules in CPI images (e.g., Korolev et al. 2004; Stith et al. 2004; Rangno 2008). Figure 8 shows examples of freezing drops suspended on fine wires, CPI images in regions with supercooled drizzle (both from Korolev et al. 2004), and Learjet CPI images captured in updrafts during ICE-T. The CPI images in Fig. 8 show frozen water drops with spicules that are very similar to those developed in the laboratory by Leisner et al. (2014). The spicules formed within a few milliseconds after initial freezing of 80-μm drops. A. V. Korolev (2014, personal communication) reports that millimeter-diameter drops took 30–40 s to emit a spicule. At the average updraft velocity of 9 m s^{-1} in ICE-T clouds, this results in about 350-m altitude gain, which is in agreement with the observations of rapid glaciation.

The CPI image in the upper-right corner of Fig. 8 resembles the laboratory image of a drop with a slushy center shown at 699.8 ms in Fig. 7a. The largest image in the first ice region shown in Fig. 6 also appears to be a drop that has just frozen and may be in the process of ejecting a spicule. The high-speed video photography does not capture all of the smallest ice particles that are ejected (Leisner et al. 2014), and several ice fragments can result from the fracturing of one bubble ejected from a spicule. Thus, even though laboratory studies estimate that only 10% of (80-μm diameter) freezing drops produce splinters, the number of ice fragments can potentially be very large.

Assuming the drop-freezing secondary ice process is active, the difference in terminal fall velocities between small ice splinters and large drops will result in frequent collisions and freezing events, potentially releasing more ice splinters. Thus, a cascading process can develop that results in rapid glaciation within the updraft (Koenig 1963). Figure 9 shows PSDs for all of the strong updraft penetrations in the temperature range between −12° and −20°C (i.e., the "rapid glaciation region" shown in Table 1). The PSDs have been separated into water (blue) and ice (red) traces based on CPI images and 2D-S images
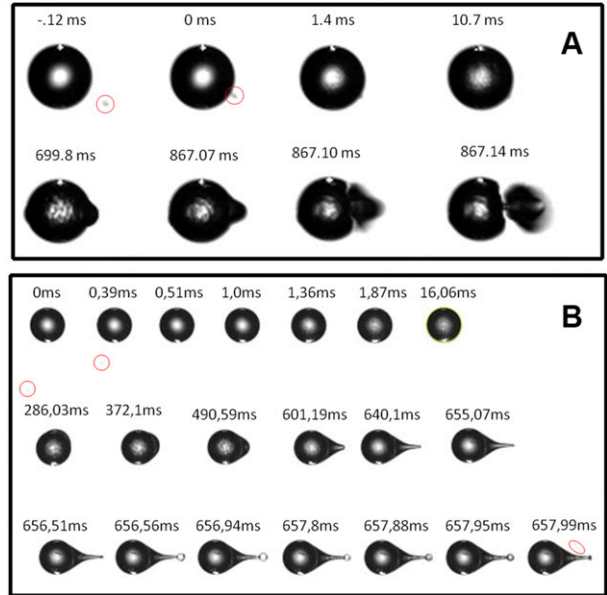

FIG. 7. (a) Example of high-speed (200 000 frames per second) photography of breakup of an 80-μm-diameter electrostatically suspended drop. (b) Example of a spicule emitting gas bubbles from an 80-μm-diameter suspended drop at −10°C. The red circles identify an ice forming nucleus entering the drop in (a) at −0.12 and 0 ms, and in (b) at 0 and 0.39 ms. The red ellipse in (b) at 657.99 ms indicates fragments from a burst bubble [adapted with permission from Leisner et al. (2014)].

for sizes larger than about 500 μm. However, as evidenced in Fig. 9, water drops with diameters larger than about 300 μm were not observed in the rapid glaciation region, which is consistent with larger drops freezing first due to their higher fall velocity relative to small ice. The average LWC decreases by about a factor of 10 and IWC increases by more than a factor of 200 in updraft cores between the first ice region and the rapid glaciation region.

The ICE-T observations provide credible support for the drop freezing–splintering process, which does not require the stringent conditions imposed by the Hallett–Mossop (H–M) ice multiplication process (Hallett and Mossop 1974). Specifically, the H–M process cannot explain the observations, because 1) the observed secondary ice production is outside the required temperature range, 2) there is not a predominance of columnar ice, and 3) the H–M process would take far too long to produce sufficient ice in these strong updrafts (Mason 1996).

3. Numerical simulations

It has been well documented in the literature that a rapid coalescence process occurs once drops with diameters larger than about 50 μm are observed in warm cumulus [e.g., see discussions in Khain et al. (2000);
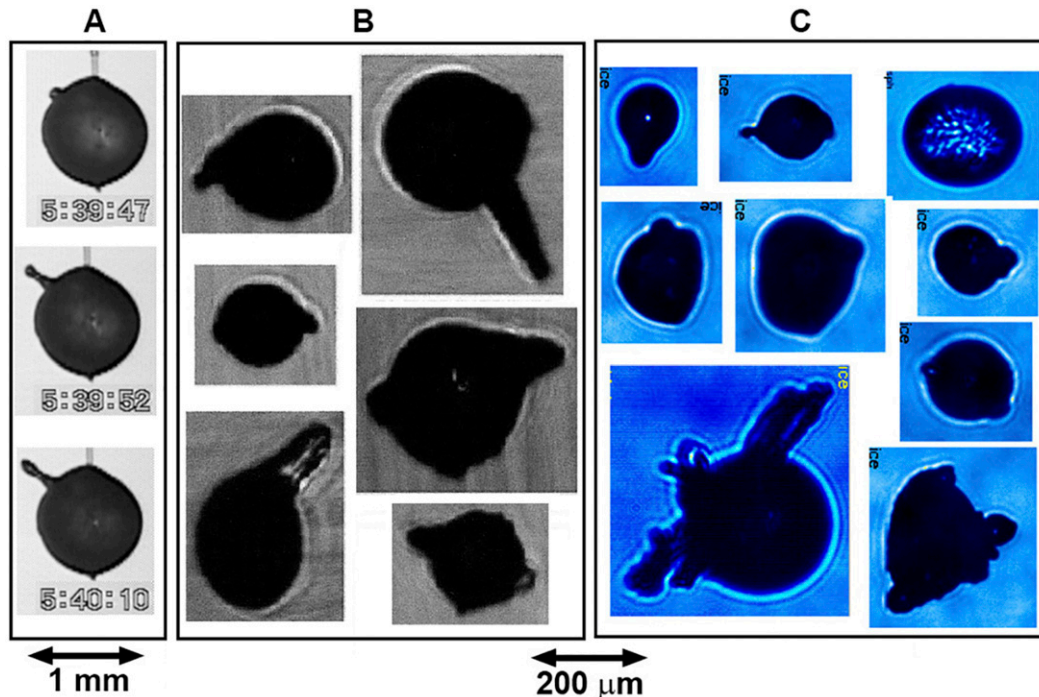
FIG. 8. (a) Example of a spicule being emitted from a millimeter-diameter drop suspended from a wire and freezing at −10°C (Korolev et al. 2004; A. V. Korolev 2014, personal communication); (b) CPI images of drops with protrusions in freezing drizzle (Korolev et al. 2004); and (c) CPI images of drops with protrusions in ICE-T clouds (present study).

Rauber et al. (2007); Alfonso et al. (2008)]. The difference in fall velocities between a millimeter drop and a 100-μm ice crystal is about $4\,\mathrm{m\,s}^{-1}$ (Khvorostyanov and Curry 2002), which will support a substantial collision rate and potential for drop freezing given a sufficient concentration of small ice. In view of the recent laboratory evidence for the drop freezing–splintering process, and in situ cloud observations showing circumstantial evidence of drop shattering and spicules, we have enlisted the aid of a numerical model to see if these processes will support rapid cloud glaciation.

The mixed-phase bin microphysics scheme of Morrison and Grabowski (2010) has been adapted to simulate the major physical components of the drop-freezing secondary ice process. This scheme predicts liquid drop and ice particle spectra by prognosing the number mixing ratios in 54 mass bins (for liquid and ice each). In addition, rime mass mixing ratios are prognosed for the ice bins, allowing for prediction of rime mass fraction and smooth transition of particle characteristics (e.g., density and fall speed) from unrimed ice to rimed particles to graupel. This is in contrast with the traditional approach that includes separate distributions for ice (snow) and graupel. Numerous processes affecting the liquid and ice spectra are represented, including diffusional growth, coalescence, riming, and secondary droplet activation. A secondary ice initiation process is

implemented based on freezing of large supercooled drops via the riming process,[3] followed by production of small ice, as described below. For this application, the scheme is configured within a 1D model with a vertical grid spacing of 50 m. Entrainment is neglected. The Meyers et al. (1992) ice nucleation, riming, and drop-freezing secondary ice processes are turned on or off to perform sensitivity tests, described later.

The model is initialized at the lowest model level, −6°C, with the observed average DSD (Fig. 4) in the observed average updraft velocity of $8\,\mathrm{m\,s}^{-1}$, constant with time and altitude. The average DSD is obtained from all ice-free updraft-core DSDs warmer than −8°C. The updraft-core average velocity of $8\,\mathrm{m\,s}^{-1}$ is the average value taken from all updraft cores, weighted by each updraft core's duration. The model ice PSD is initialized with the observed average first ice PSD (Fig. 5) between −8° and −11°C at 10-s intervals between 100 and 160 s. The frequency of introduction of the first ice PSD in the ice initiation region is arbitrary and was established experimentally to fit the initial observations.

---

[3] Here, riming is the freezing event when a small ice particle collides with a larger supercooled drop, which could be considered the reverse of the classic process of a small supercooled drop accreting on a larger ice particle.
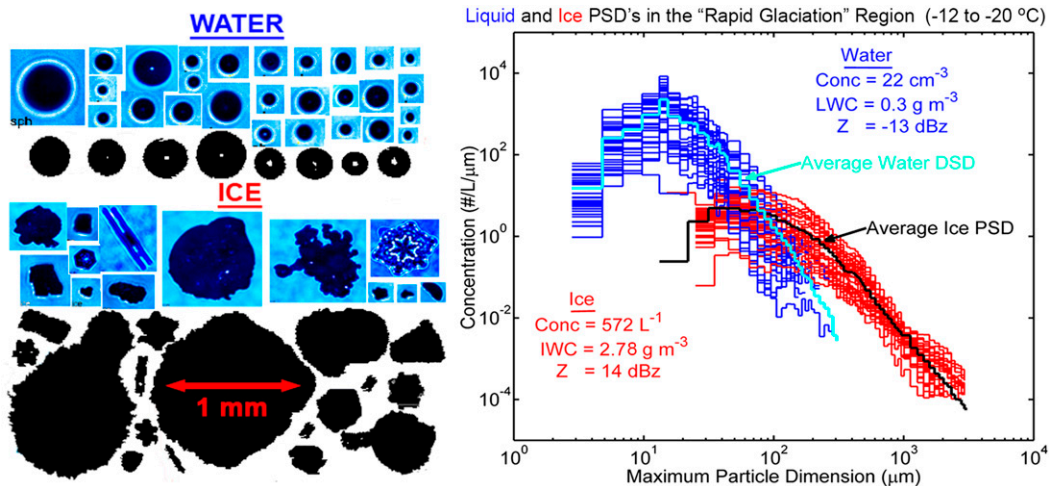
FIG. 9. As in Fig. 5, but for the rapid glaciation region shown in Table 1; examples of both CPI and 2D-S images are shown.

The purpose of this study is *not* to identify the source of the first ice, which could possibly result from various mechanisms. That said, a few possibilities for first ice will be mentioned here to stimulate further discussion. The presence of millimeter-diameter drops increases the statistical probability that a rare ice nucleus might be active within these large drops within a relatively warm ($-8°$ to $-11°C$) temperature regime, since the probability of containing an active ice nucleus increases with the cube of the drop radius. The most likely candidates are biogenic ice nuclei, which are known to have some activity at these warmer temperatures and have been observed over open ocean (Burrows et al. 2013). Alternatively, a millimeter-diameter drop may break up and produce ice particles. Or, although unlikely in these clouds that are selected to be relatively isolated above the 0°C level, ice could be entrained from outside the cloud. What is apparent is that once there are even a few freezing events, the drop-freezing secondary ice mechanism rapidly takes over and a cascading glaciation process dominates.

In the model, the differential fall velocity between the ice particles and water drops promotes collisions and freezing of supercooled drops, which then produce secondary ice particles at a rate commensurate with the observed ice PSD at that level in the updraft; that is, the rate of secondary ice production is calculated so that the ice PSD is nudged toward the observed PSD. This process and an estimate of the rate of ice fragment production are discussed in more detail later in this section. The secondary ice production results in conversion of more water drops to ice so that the model DSD adjusts toward the observed DSD. The process continues until the updraft reaches $-20°C$. The overall goals of the simulation are as follows: 1) to see if the observed water DSDs and ice PSDs can be generated in the model through the drop-freezing secondary ice production and riming processes that occur when large drops collide with small ice particles, and 2) to determine the number of ice fragments required through the riming process for consistency with the observed water DSDs and ice PSDs.

Figure 10 shows results from the numerical simulation without the drop-freezing secondary ice process. In this realization, the model is initiated with the observed DSD at $-6°C$ in an updraft of $8 m s^{-1}$. The warm-rain coalescence process is active. The model ice PSD is initialized with the observed average first ice PSD between $-8°$ and $-11°C$ at 10-s intervals between 100 and 160 s. Drops are frozen via the Meyers immersion-freezing and deposition scheme and through riming, but there is no secondary ice production process. Ice grows via vapor deposition and riming. As seen in Fig. 10, there are one to two orders of magnitude higher drop concentrations in the model DSD at $-12°$ and $-16°C$, and the tail extends a millimeter past the observations. The model ice PSD is orders of magnitude lower than the average observed ice PSD. To summarize, 50-μm- to 3-mm-diameter water drops in the model do not freeze in the updraft at nearly the rate as the observed ice PSD.

In contrast, Fig. 11 shows the development of the water DSDs and ice PSDs when the drop-freezing (fracturing) secondary ice process is turned on. In this realization, the model is initialized the same way as in Fig. 10, but the primary ice nucleation (Meyers) processes are turned off, and the drop-freezing secondary ice process is turned on. Secondary ice particles are generated when drops $>80 \mu$m freeze, and supercooled drops freeze whenever they come in contact with ice particles (i.e., the riming process). The lower drop-diameter limit of 80μm is estimated from the laboratory
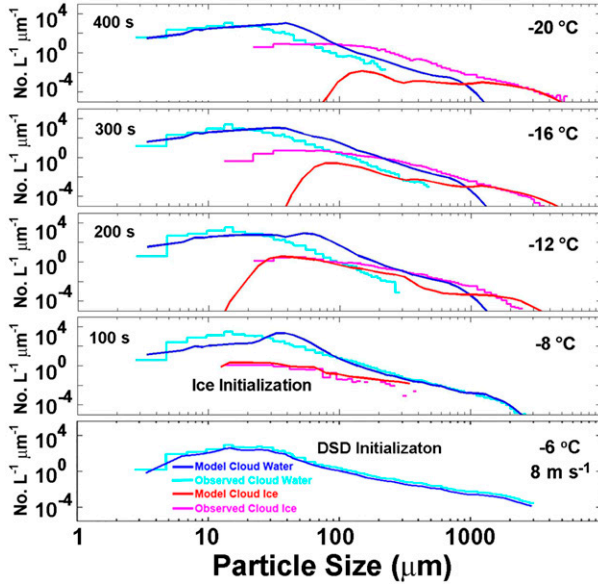
FIG. 10. Model simulations showing the development of water DSD and ice PSD compared with average ICE-T observations. Model is initialized at −6°C with the observed DSD in a constant 8 m s^{-1} updraft. At −8°C the ICE-T observed ice PSD is introduced. Meyers et al. (1992) primary nucleation and the riming processes are turned on; secondary ice production is turned off.
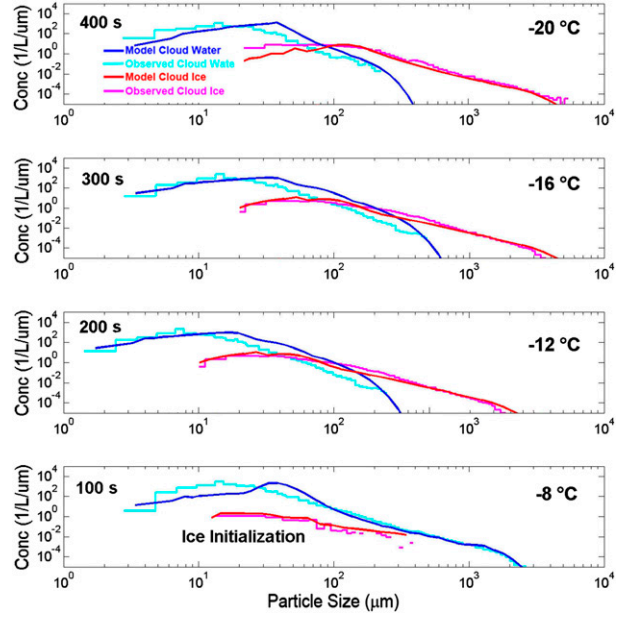

FIG. 11. As in Fig. 10, but the drop-freezing secondary ice process is turned on, and the Meyers et al. (1992) primary nucleation scheme is turned off.

work of Leisner et al. (2014). As stated above, one of the goals of the model is to see if the observed water DSDs and ice PSDs can be reproduced in the model and to determine the relationship between the diameter of freezing drops and the number of ice particles produced.

The scheme for determining how much secondary ice is required to force the development of ice and depletion of liquid water in the model to agree with the observations proceeds as follows. Drops in the model that are frozen via the riming process may or may not fracture and produce secondary ice particles. Secondary ice particles are produced by multiplying the mixing ratio of liquid mass that is frozen by a fragmentation factor F, which is the number of secondary ice particles per kilogram of accumulated rime mass. The secondary ice produced is distributed evenly over a range of ice size bins that are smaller than the diameter of the original frozen drop. The resulting DSDs and ice PSDs are then compared with the observations, and the fragmentation factor F is iteratively varied to optimize the agreement between the model and observed DSDs and ice PSDs over 300 s, the time it takes the model updraft to rise from the −8° to −20°C level. The optimal value of F is 10^{-9} kg^{-1}.

The average number of secondary ice particles produced as a function of fractured frozen-drop diameter is shown in the scatterplot in Fig. 12, which is derived from

the model. Note that the results shown in Fig. 12 are a statistical average. For example, from the curve in Fig. 12 it can be seen that a drop with a diameter of about 500 μm can fracture and produce five secondary ice particles. Or alternatively, one out of one hundred 500-μm drops could fracture and produce 500 secondary ice fragments. There is no way of determining in the model how many individual drops do or do not fragment. A power law fit to the points in Fig. 12 results in $N_f = 2.5 \times 10^{-11} d^4$, where N_f is the statistical average number of ice fragments per drop, and d is drop diameter in micrometers.
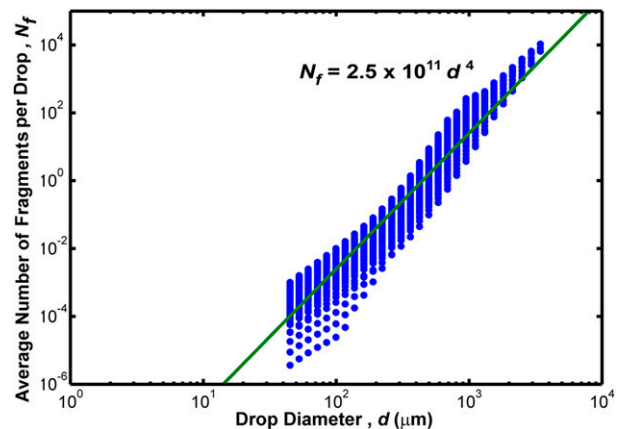

FIG. 12. Scatterplot derived from model results showing the statistically averaged number of secondary ice fragments per frozen drop N_f as a function of binned drop diameter d.

As seen in Fig. 7, 80-μm-diameter drops freeze and fracture in a fraction of a second. However, millimeter-diameter drops take longer to freeze and produce a spicule. Based on laboratory work performed by Korolev et al. (2004) and estimates by A. V. Korolev (2014, personal communication), it takes about 30 s to produce a spicule from a 1-mm-diameter drop. Thus, in the actual cloud, millimeter drops can be transported about 100–200 m vertically, either up or down depending on updraft and terminal drop velocities, before producing secondary ice.

In addition to turning on/off primary nucleation, secondary nucleation, and riming, sensitivity tests were conducted to determine how other model parameters affected the results. Updraft velocity was varied over a range from 5 to 15 m s^{-1}, and updraft velocity was also varied as a function of time. To freeze supercooled drops at a rate commensurate with the observations, updraft velocity needs to be in the range from about 7 to 10 m s^{-1}, and small velocity variations with time do not greatly affect the results. If updraft velocity is less than about 5 m s^{-1}, the largest drops precipitate out of the updraft and are not frozen, resulting in less than observed ice development. If updraft velocity is greater than about 15 m s^{-1}, supercooled drops are converted to ice at a higher elevation than observed in ICE-T clouds.

Model runs were also conducted by varying the initialized DSD and the initial ice PSD. If the DSD at -6°C does not contain drops larger than about 200 μm in diameter, the conversion to ice via drop-freezing secondary ice production and riming is greatly diminished, resulting in less ice and more supercooled water being transported higher in the cloud. Varying the initial ice PSD by increasing or decreasing ice in the first ice region by an order of magnitude had little effect on subsequent development of the ice PSD higher in the cloud. This implies that once the drop-freezing secondary ice process gets started, there is a cascading production of small ice that rapidly freezes larger drops via the riming process.

4. Summary and conclusions

Data collected by the SPEC Learjet and the NCAR C-130 from the Ice in Clouds Experiment–Tropical (ICE-T) are analyzed to assess the mechanism(s) that produce(s) rapid glaciation between -8° and -15°C in strong updrafts. The tropical cumulus clouds studied formed over the open ocean near St. Croix in July 2011. Based on 31 aircraft penetrations within 200 m above cloud base, the average drop size distribution (DSD) contained drops out to diameters of 80 μm, and the total drop concentration was about 85 cm^{-3}. The average cloud-base temperature was 22°C. The measurements reported here are constrained to relatively strong updrafts within

individual cloud turrets (i.e., the edges of updrafts are not included). The average updraft velocity between 5° and -8°C was 9.5 m s^{-1}; between -8° and -12°C it was 10.3 m s^{-1}; and it was 7.4 m s^{-1} between -12° and -20°C. Much stronger 1-s peak updrafts were encountered at all levels: 23 m s^{-1} at -7°C, 25.4 m s^{-1} at -11°C, and 21 m s^{-1} at -20°C.

A very active coalescence process was observed within all of the updrafts and often produced millimeter-diameter drops at the level when cloud-base air reached the 5°C level. The concentration and size of millimeter drops increased until glaciation commenced. The first ice region, based on ICE-T measurements, was found in the temperature range from about -8° to -11°C. The first ice particles are irregular in shape, sometimes appearing to be fragments of a drop, and were measured in the size range from about 50 to 200 μm. Once the first ice is observed, the updraft rapidly glaciates within about 1–1.5-km upward vertical development, which corresponds to approximately a 6°–9°C decrease in temperature within a time frame of 2–3 min. The Learjet was able to climb at a rate that allowed it to sample 1–1.5 km higher in the same updraft within about 3 min, thereby enabling it to document the rapid glaciation (Fig. 2). CPI and 2D-S images showed that the large tail of the water DSD was quickly depleted during the rapid glaciation process, the millimeter-size images appearing to be large frozen drops and graupel particles. That is, the tail of the DSD, which originally extended out to 3 mm in the first ice region (-8° to -11°C) decreased to about 300 μm in the rapid glaciation region (-12° to -20°C).

Leisner et al. (2014) show high-speed photography of suspended 80-μm-diameter drops freezing in the -10° to -20°C temperature range. More than 10% of the freezing drops break up into fragments or produce spicules that emit liquid bubbles, which subsequently burst and produce ice fragments. This is the first strong laboratory evidence for the drop-freezing secondary ice production process suggested by investigators in the 1950s (i.e., Bigg 1957; Latham and Mason 1961; Koenig 1963, 1965), which is corroborated by CPI images collected by aircraft in clouds (Korolev et al. 2004; Rangno 2008; present study). Both of these processes are capable of producing multiple secondary ice particles during a single drop-freezing event. The difference in fall velocity between small ice particles and large supercooled drops results in a riming process whereby large drops freeze on contact with the small ice. This in turn produces secondary ice particles, which freeze more supercooled drops, resulting in a cascading process that rapidly glaciates the cloud.

The Morrison and Grabowski (2010) mixed-phase bin model was modified to determine if the riming and

drop-freezing secondary ice production process can account for the observations of rapid glaciation in ICE-T clouds. The modified microphysics scheme was implemented into a 1D cloud model. An $8\,\mathrm{m\,s}^{-1}$ updraft was initiated with the observed water DSD at $-6°C$ and the observed ice PSD between $-8°$ and $-11°C$. Warm coalescence and the drop-freezing secondary ice process were simulated, and riming was turned on. The model showed that the observed rapid glaciation was simulated when drops between $40\,\mu m$ and $1\,mm$ froze via riming and emitted secondary ice in proportion to their diameter (mass). The glaciation process proceeds rapidly because of large differences in fall velocity between small ice and large drops. Turning on or off the Meyers et al. (1992) primary nucleation process had minimal effect.

ICE-T in situ observations, supported by recent laboratory evidence of drop splintering, spicule formation, and numerical simulations, strongly support the premise that drop freezing produces small secondary ice particles, which collide with larger drops and account for the observed rapid glaciation in strong updrafts of tropical cumulus clouds. It is worthwhile to reflect on the hypothesis put forth by Koenig (1965, p. 448) over 50 years ago: "The [secondary ice] mechanism can only be effective in cases when clouds contain large supercooled drops. It is believed that the hypothesized mechanism may supply a critical link in the understanding of cloud glaciation by providing a means of triggering the avalanche mechanism involving ice splinter formation during drop freezing."

REFERENCES

Alfonso, L., G. B. Raga, and D. Baumgardner, 2008: The validity of the kinetic collection equation revisited. *Atmos. Chem. Phys.,* **8,** 969–982, doi:10.5194/acp-8-969-2008.

Anderson, N. F., C. A. Grainger, and J. L. Stith, 2005: Characteristics of strong updrafts in precipitation systems over the central tropical Pacific Ocean and in the Amazon. *J. Appl. Meteor.,* **44,** 731–738, doi:10.1175/JAM2231.1.

Baker, B. A., and R. P. Lawson, 2006: Improvement in determination of ice water content from two-dimensional particle imagery. Part I: Image-to-mass relationships. *J. Appl. Meteor. Climatol.,* **45,** 1282–1290, doi:10.1175/JAM2398.1.

Beard, K., 1992: Ice initiation in warm-base convective clouds: An assessment of microphysical mechanisms. *Atmos. Res.,* **28,** 125–152, doi:10.1016/0169-8095(92)90024-5.

Beswick, K. M., M. W. Gallagher, A. R. Webb, E. G. Norton, and F. Perry, 2008: Application of the Aventech AIMMS20AQ airborne probe for turbulence measurements during the Convective Storm Initiation Project. *Atmos. Chem. Phys.,* **8,** 5449–5463, doi:10.5194/acp-8-5449-2008.

Bigg, E. K., 1957: The fragmentation of freezing water drops. *Bull. Obs. Puy de Dome,* 65–69.

Brenguier, J.-L., T. Bourrianne, A. de Araujo Coelho, J. Isbert, R. Peytavi, D. Trevarin, and P. Wechsler, 1998: Improvements of droplet size distribution measurements with the Fast-FSSP. *J. Atmos. Oceanic Technol.,* **15,** 1077–1090, doi:10.1175/1520-0426(1998)015<1077:IODSDM>2.0.CO;2.

Burrows, S. M., C. Hoose, U. Pöschl, and M. G. Lawrence, 2013: Ice nuclei in marine air: Biogenic particles or dust? *Atmos. Chem. Phys.,* **13,** 245–267, doi:10.5194/acp-13-245-2013.

Cotton, W. R., 1972a: Numerical simulation of precipitation development in supercooled cumuli—Part I. *Mon. Wea. Rev.,* **100,** 757–763, doi:10.1175/1520-0493(1972)100<0757:NSOPDI>2.3.CO;2.

——, 1972b: Numerical simulation of precipitation development in supercooled cumuli—Part II. *Mon. Wea. Rev.,* **100,** 764–784, doi:10.1175/1520-0493(1972)100<0764:NSOPDI>2.3.CO;2.

Hallett, J., and S. C. Mossop, 1974: Production of secondary ice particles during the riming process. *Nature,* **249,** 26–28, doi:10.1038/249026a0.

——, R. I. Sax, D. Lamb, and A. S. R. Murty, 1978: Aircraft measurements of ice in Florida cumuli. *Quart. J. Roy. Meteor. Soc.,* **104,** 631–651, doi:10.1002/qj.49710444108.

Harris-Hobbs, R. L., and W. A. Cooper, 1987: Field evidence supporting quantitative predictions of secondary ice production rates. *J. Atmos. Sci.,* **44,** 1071–1082, doi:10.1175/1520-0469(1987)044<1071:FESQPO>2.0.CO;2.

Heymsfield, A. J., and P. Willis, 2014: Cloud conditions favoring secondary ice particle production in tropical maritime convection. *J. Atmos. Sci.,* **71,** 4500–4526, doi:10.1175/JAS-D-14-0093.1.

Heymsfield, G. M., L. Tian, A. J. Heymsfield, L. Li, and S. Guimond, 2010: Characteristics of deep tropical and subtropical convection from nadir-viewing high-altitude airborne Doppler radar. *J. Atmos. Sci.,* **67,** 285–308, doi:10.1175/2009JAS3132.1.

Hobbs, P. V., and A. L. Rangno, 1985: Ice particle concentrations in clouds. *J. Atmos. Sci.,* **42,** 2523–2549, doi:10.1175/1520-0469(1985)042<2523:IPCIC>2.0.CO;2.

——, and ——, 1990: Rapid development of high ice particle concentrations in small polar maritime cumuliform clouds. *J. Atmos. Sci.,* **47,** 2710–2722, doi:10.1175/1520-0469(1990)047<2710:RDOHIP>2.0.CO;2.

Khain, A. P., M. Ovtchinnikov, M. Pinsky, A. Pokrovsky, and H. Krugliak, 2000: Notes on the state-of-the-art numerical modeling of cloud microphysics. *Atmos. Res.,* **55,** 159–224, doi:10.1016/S0169-8095(00)00064-8.

Khvorostyanov, V. I., and J. A. Curry, 2002: Terminal velocities of droplets and crystals: Power laws with continuous parameters over the size spectrum. *J. Atmos. Sci.,* **59,** 1872–1884, doi:10.1175/1520-0469(2002)059<1872:TVODAC>2.0.CO;2.

Koenig, L. R., 1963: The glaciating behavior of small cumulonimbus clouds. *J. Atmos. Sci.,* **20,** 29–47, doi:10.1175/1520-0469(1963)020<0029:TGBOSC>2.0.CO;2.

——, 1965: Drop freezing through drop breakup. *J. Atmos. Sci.,* **22,** 448–451, doi:10.1175/1520-0469(1965)022<0448:DFTDB>2.0.CO;2.

Korolev, A. V., 2007: Reconstruction of the sizes of spherical particles from their shadow images. Part I: Theoretical considerations. *J. Atmos. Oceanic Technol.,* **24,** 376–389, doi:10.1175/JTECH1980.1.

——, M. P. Bailey, J. Hallett, and G. A. Isaac, 2004: Laboratory and in situ observation of deposition growth of frozen drops. *J. Appl. Meteor.,* **43,** 612–622, doi:10.1175/1520-0450(2004)043<0612:LAISOO>2.0.CO;2.

——, E. F. Emery, J. W. Strapp, S. G. Cober, G. A. Isaac, M. Wasey, and D. Marcotte, 2011: Small ice particles in tropospheric clouds: Fact or artifact? Airborne icing instrumentation evaluation experiment. *Bull. Amer. Meteor. Soc.,* **92,** 967–973, doi:10.1175/2010BAMS3141.1.

Kuettner, J. P., 1974: General description and central program of GATE. *Bull. Amer. Meteor. Soc.,* **55,** 712–719.

——, and D. E. Parker, 1976: GATE: Report on the field phase. *Bull. Amer. Meteor. Soc.,* **55,** 11–27.

Lance, S., C. A. Brock, D. Rogers, and J. A. Gordon, 2010: Water droplet calibration of a cloud droplet probe and in-flight performance in liquid, ice and mixed-phase clouds during ARCPAC. *Atmos. Meas. Tech.,* **3,** 1683–1706, doi:10.5194/amt-3-1683-2010.

Latham, J., and B. J. Mason, 1961: Generation of electric charge associated with the formation of soft hail in thunderclouds. *Proc. Roy. Soc. London,* **A260,** 537–549, doi:10.1098/rspa.1961.0052.

Lawson, R. P., 2011: Effects of ice particles shattering on the 2D-S probe. *Atmos. Meas. Tech.,* **4,** 1361–1381, doi:10.5194/amt-4-1361-2011.

——, and W. A. Cooper, 1990: Performance of some airborne thermometers in clouds. *J. Atmos. Oceanic Technol.,* **7,** 480–494, doi:10.1175/1520-0426(1990)007<0480:POSATI>2.0.CO;2.

——, and P. Zuidema, 2009: Aircraft microphysical and surface-based radar observations of summertime Arctic clouds. *J. Atmos. Sci.,* **66,** 3505–3529, doi:10.1175/2009JAS3177.1.

——, R. E. Stewart, and L. J. Angus, 1998: Observations and numerical simulations of the origin and development of very large snowflakes. *J. Atmos. Sci.,* **55,** 3209–3229, doi:10.1175/1520-0469(1998)055<3209:OANSOT>2.0.CO;2.

——, B. A. Baker, C. G. Schmitt, and T. L. Jensen, 2001: An overview of microphysical properties of Arctic clouds observed in May and July during FIRE ACE. *J. Geophys. Res.,* **106,** 14 989–15 014, doi:10.1029/2000JD900789.

——, D. O'Connor, P. Zmarzly, K. Weaver, B. A. Baker, Q. Mo, and H. Jonsson, 2006: The 2D-S (stereo) probe: Design and preliminary tests of a new airborne, high speed, high-resolution particle imaging probe. *J. Atmos. Oceanic Technol.,* **23,** 1462–1477, doi:10.1175/JTECH1927.1.

Leisner, T., T. Pander, P. Handmann, and A. Kiselev, 2014: Secondary ice processes upon heterogeneous freezing of cloud droplets. *14th Conf. on Cloud Physics and Atmospheric Radiation,* Boston, MA, Amer. Meteor. Soc., 2.3. [Available online at https://ams.confex.com/ams/14CLOUD14ATRAD/webprogram/Paper250221.html.]

LeMone, M. A., 1980: On the difficulty of measuring temperature and humidity in cloud: Comments on "Shallow convection on day 261 of GATE: Mesoscale arcs." *Mon. Wea. Rev.,* **108,** 1702–1705, doi:10.1175/1520-0493(1980)108<1703:OTDOMT>2.0.CO;2.

Lucas, C., E. J. Zipser, and M. A. Lemone, 1994: Vertical velocity in oceanic convection off tropical Australia. *J. Atmos. Sci.,* **51,** 3183–3193, doi:10.1175/1520-0469(1994)051<3183:VVIOCO>2.0.CO;2.

Malkus, J., 1954: Some results of a trade-cumulus cloud investigation. *J. Meteor.,* **11,** 220–237, doi:10.1175/1520-0469(1954)011<0220:SROATC>2.0.CO;2.

——, 1957: Trade cumulus cloud groups: Some observations suggesting a mechanism of their origin. *Tellus,* **9A,** 33–44, doi:10.1111/j.2153-3490.1957.tb01851.x.

——, and C. Ronne, 1954: On the structure of some cumulonimbus which penetrated the high tropical atmosphere. *Tellus,* **6A,** 351–366, doi:10.1111/j.2153-3490.1954.tb01130.x.

Mason, B. J., 1996: The rapid glaciation of slightly supercooled cumulus clouds. *Quart. J. Roy. Meteor. Soc.,* **122,** 357–365, doi:10.1002/qj.49712253003.

Meyers, M. P., P. J. DeMott, and W. R. Cotton, 1992: New primary ice-nucleation parameterizations in an explicit cloud model. *J. Appl. Meteor.,* **31,** 708–721, doi:10.1175/1520-0450(1992)031<0708:NPINPI>2.0.CO;2.

Morrison, H., and W. W. Grabowski, 2010: An improved representation of rimed snow and conversion to graupel in a multicomponent bin microphysics scheme. *J. Atmos. Sci.,* **67,** 1337–1360, doi:10.1175/2010JAS3250.1.

Mossop, S. C., 1968: Comparison between concentration of ice crystals in cloud and the concentration of ice nuclei. *J. Rech. Atmos.,* **3,** 119–124.

——, A. Ono, and E. R. Wishart, 1970: Ice particles in maritime clouds near Tasmania. *Quart. J. Roy. Meteor. Soc.,* **96,** 487–508, doi:10.1002/qj.49709640910.

O'Connor, D., B. Baker, and R. P. Lawson, 2008: Upgrades to the FSSP-100 Electronics. *15th. Int. Conf. on Clouds and Precipitation.* Cancun, Mexico, Universidad Nacional Autónoma de México, P13.6. [Available online at http://cabernet.atmosfcu.unam.mx/ICCP-2008/abstracts/Program_on_line/Poster_13/O-Connor_extended_final.pdf.]

Pruppacher, H. R., and J. D. Klett, 1997: *Microphysics of Clouds and Precipitation.* Kluwer Academic Publishers, 954 pp.

Rangno, A. L., 2008: Fragmentation of freezing drops in shallow maritime frontal clouds. *J. Atmos. Sci.,* **65,** 1455–1466, doi:10.1175/2007JAS2295.1.

Rauber, R. M., and Coauthors, 2007: Rain in shallow cumulus over the ocean: The RICO campaign. *Bull. Amer. Meteor. Soc.,* **88,** 1912–1928, doi:10.1175/BAMS-88-12-1912.

Rodenhuis, D. R., 1974: The Convection Subprogram. *Bull. Amer. Meteor. Soc.,* **55,** 724–730.

Scott, B. C., and P. V. Hobbs, 1977: A theoretical study of the evolution of mixed-phase cumulus clouds. *J. Atmos. Sci.,* **34,** 812–826, doi:10.1175/1520-0469(1977)034<0812:ATSOTE>2.0.CO;2.

Simpson, J., R. H. Simpson, D. A. Andrews, and M. A. Eaton, 1965: Experimental cumulus dynamics. *Rev. Geophys.,* **3,** 387–431, doi:10.1029/RG003i003p00387.

Stith, J. L., J. A. Haggerty, A. Heymsfield, and C. A. Grainger, 2004: Microphysical characteristics of tropical updrafts in clean conditions. *J. Appl. Meteor.,* **43,** 779–794, doi:10.1175/2104.1.